**Original Research**

# Comparative Study of Methods for Determining Vascular Permeability and Blood Volume in Human Gliomas

Judith U. Harrer, MD,[1] Geoff J.M. Parker, PhD,[2] Hamied A. Haroon, MSc,[2] David L. Buckley, PhD,[2] Karl Embelton, MSc,[2] Caleb Roberts, BSc,[2] Danielle Balériaux, MD,[3] and Alan Jackson, MBChB, PhD[2]*

**Purpose:** To characterize human gliomas using $T_1$-weighted dynamic contrast-enhanced MRI (DCE-MRI), and directly compare three pharmacokinetic analysis techniques: a conventional established technique and two novel techniques that aim to reduce erroneous overestimation of the volume transfer constant between plasma and the extravascular extracellular space (EES) ($K^{trans}$) in areas of high blood volume.

**Materials and Methods:** Eighteen patients with high-grade gliomas underwent DCE-MRI. Three kinetic models were applied to estimate $K^{trans}$ and fractional blood plasma volume ($v_p$). We applied the Tofts and Kermode (TK) model without arterial input function (AIF) estimation, the TK model modified to include $v_p$ and AIF estimation (mTK), and a "first pass" variant of the TK model (FP).

**Results:** $K_{TK}$ values were considerably higher than $K_{mTK}$ and $K_{FP}$ values ($P < 0.001$). $K_{mTK}$ and $K_{FP}$ were more comparable and closely correlated ($\rho = 0.744$), with $K_{mTK}$ generally higher than $K_{FP}$ ($P < 0.001$). Estimates of $v_{p(mTK)}$ and $v_{p(FP)}$ also showed a significant difference ($P < 0.001$); however, these values were very closely correlated ($\rho = 0.901$). $K_{TK}$ parameter maps showed "pseudopermeability" effects displaying numerous vessels. These were not visualized on $K_{mTK}$ and $K_{FP}$ maps but appeared on the corresponding $v_p$ maps, indicating a failure of the TK model in commonly occurring vascular regions.

**Conclusion:** Both of the methods that incorporate a measured AIF and an estimate of $v_p$ provide similar pathophysiological information and avoid erroneous overestimation of $K^{trans}$ in areas of significant vessel density, and thus allow a more accurate estimation of endothelial permeability.

**Key Words:** dynamic contrast-enhanced MRI; brain tumor; permeability measurements; blood–brain barrier; perfusion imaging; cerebral blood volume
**J. Magn. Reson. Imaging 2004;20:748–757.**


TUMOR MICROVASCULATURE is characterized by a disproportionate fraction of blood vessels in comparison to the tissue fraction, abnormal vessel morphology and routing, and altered blood flow. Of particular interest is the endothelial permeability of the newly developed vessels, since these characteristically show large intercellular gaps that allow the passage of medium- and large-sized molecules from the intravascular to the extravascular extracellular space (EES) (1,2).

Several pharmacokinetic parameters, such as the volume transfer constant ($K^{trans}$) between plasma and the EES, the fractional volumes of the EES ($v_e$), and the plasma ($v_p$) can be derived from contrast agent (CA) concentration curves obtained from $T_1$-weighted dynamic contrast-enhanced MRI (DCE-MRI) after fitting a pharmacokinetic model of CA distribution (3–7). Of the various different approaches to analyze DCE-MRI data, the most commonly applied is the Tofts and Kermode (TK) model described in 1991, which is based on an assumed arterial input function (AIF) that is derived from a sample of the normal population (3). Its wide use is most likely explained by its excellent stability and simplicity of application (8,9). However, this technique has been shown to be subject to a number of potential errors. One problem is the assumption that the observed CA concentration change in each voxel solely reflects CA leakage into the EES. This leads to erroneously high $K^{trans}$ values caused by intravascular CA, which itself contributes to the signal increase that often affects many voxels (10–13). This artifact has therefore been referred to as "pseudopermeability." Another cause of error in the conventional TK model is the application of a standardized vascular input function

[1]Department of Neurology, Aachen University Hospital, Aachen, Germany.
[2]Imaging Science and Biomedical Engineering, University of Manchester, Manchester, UK.
[3]Service de Radiologie, Hôpital Erasme, Cliniques Universitaires de Bruxelles, Bruxelles, Belgium.
Contract grant sponsor: German Society of Clinical Neurophysiology and Functional Imaging.
*Address reprint requests to: A.J., Imaging Science and Biomedical Engineering, Faculty of Medicine, University of Manchester, Stopford Building, Oxford Road, Manchester, M13 9PT, United Kingdom.E-mail: Alan.Jackson@man.ac.uk
Received February 2, 2004; Accepted June 23, 2004.
DOI 10.1002/jmri.20182
Published online in Wiley InterScience (www.interscience.wiley.com).

Table 1
Abbreviations of Pharmacokinetic Variables

| Symbol | Definition | Units |
|---|---|---|
| EES | Extracellular extravascular space | None |
| $K^{trans}$ | Volume transfer constant between plasma and EES | $min^{-1}$ |
| $K_{TK}$ | $K^{trans}$ analyzed according to Tofts and Kermode's model | $min^{-1}$ |
| $K_{mTK}$ | $K^{trans}$ analyzed according to the modified Tofts and Kermode's model | $min^{-1}$ |
| $K_{FP}$ | $K^{trans}$ analyzed according to the first-pass model | $min^{-1}$ |
| $v_e$ | Volume of EES per unit volume of tissue | None |
| $v_{e(TK)}$ | $v_e$ analyzed according to Tofts and Kermodes model | None |
| $v_{e(mTK)}$ | $v_e$ analyzed according to the modified Tofts and Kermode's model | None |
| $v_p$ | Blood plasma volume per unit volume of tissue | None |
| $v_{p(FP)}$ | *vp* analyzed according to the first-pass model | None |
| $v_{p(mTK)}$ | *vp* analyzed according to the modified Tofts and Kermode's model | None |
| $C_e$ | Extravascular extracellular component of C(t), which equals tracer concentration in plasma multiplied by $v_e$ | mmol |
| $C_p$ | Tracer concentration in arterial blood plasma | mmol |
| $C_v$ | Intravascular component of C(t), which equals tracer concentration in plasma multiplied by $v_p$ | mmol |
| C(t) | Concentration of the contrast medium in the voxel at time t | mmol |

(VIF) that ignores the first-pass effect resulting from the CA bolus, and misses interindividual physiological differences (14,15). The shortcomings of the TK model reflect its original application in multiple sclerosis, where there is little contribution from intravascular contrast to the signal enhancement (3,8).

To overcome these problems, modifications were made to the TK model, the most important being the consideration of the signal contribution of the intravascular tracer (4,10,16). The use of such an approach in combination with a patient-specific VIF enables one to separate vascular and nonvascular contributions to the enhancement of each voxel. By analyzing a DCE $T_1$ image series with this method, one can calculate $K^{trans}$, $v_e$, and $v_p$. This method has been applied in a range of tumors, including breast and lung cancers, in addition to other vascular pathologies (5,8).

Li et al (20) introduced a simplification of this approach that is based on the leakage profile during the first passage of the CA bolus. Their method, termed the first-pass leakage profile (FPLP) method, requires only the first passage period of the CA concentration time series to be measured, but does not allow an estimate of $v_e$ to be made. Studies on simulated data, in patients with hepatic tumors and primary brain tumors have proven the high reproducibility of this method (17–20). Furthermore, it has been demonstrated that this new technique has a high resistance to noise, and is particularly useful when the signal-to-noise-ratio (SNR) is low (17–20). Despite the advantage that data acquisition requires only 1–2 minutes, this model also has shortcomings due to the assumption that CA backflow from EES to plasma is negligible during the first pass of the CA bolus, and therefore $v_e$ cannot be estimated. This leads to a systematic underestimation of $K^{trans}$ values where CA extraction fractions are high (18,19).

Given two different models that were designed to overcome pseudopermeability effects, we aimed to compare the modified TK model and the FPLP method systematically in a group of patients with primary brain tumors and to compare both with the conventional TK technique. Patients with high-grade gliomas were chosen because this is the most common type of malignant brain tumor in adults, and typically presents with a high degree of CA leakage to the EES due to the breakdown of the blood–brain barrier (BBB).

## MATERIALS AND METHODS

See Table 1 for the definition of terms and symbols; the terminology used follows the conventions described by Tofts et al (6).

### *Patients*

Patients were recruited from the Neurosurgical Clinic at the Central Manchester Healthcare Trust and the Service de Radiologie, Hôpital Erasme, Clinique Universitaires de Bruxelles, from 1999 to 2002. The study was approved by the medical ethics committees at both centers, and all patients gave written informed consent. Eighteen patients (13 males and five females, mean age = 55.5 years, range = 36–75 years) with histologically proven high-grade glioma were included in the study. Of these, three patients had an anaplastic glioma (WHO grade III) and 15 had a glioblastoma multiforme (WHO grade IV). All of the patients underwent a complete physical and neurological examination, routine blood tests, and contrast-enhanced CT or MRI prior to this study. All of the patients were treated with oral dexamethasone (4 mg four times per day) from the time of diagnosis. Table 2 summarizes the demographic and clinical data of the patients.

### *Scanning Protocol*

Imaging was performed on a 1.5 Tesla ACS Gyroscan NT-PT 6000 (Philips Medical Systems, Best, The Netherlands) with a maximum gradient strength of 23 mT/m and a maximum slew rate of 105 mT $m^{-1}$ using a birdcage head coil. A 16-G catheter was inserted into an antecubital vein before scanning was conducted. Routine $T_1$- and $T_2$-weighted imaging preceded the dynamic studies. Dynamic contrast-enhanced (DCE) studies

Table 2
Demographic Data, Tumor Histology, and Tumor Localization of 18 Patients

| No. | Age | Sex | Tumor histology | Location |
|---|---|---|---|---|
| 1 | 58 | M | Glioblastoma multiforme | Left temporal |
| 2 | 46 | F | Anaplastic astrocytoma | Left basal ganglia |
| 3 | 75 | M | Anaplastic astrocytoma | Left temporo-parietal |
| 4 | 55 | M | Glioblastoma multiforme | Right temporal |
| 5 | 52 | M | Glioblastoma multiforme | Left frontal |
| 6 | 53 | M | Anaplastic astrocytoma | Right temporal |
| 7 | 53 | M | Glioblastoma multiforme | Left parieto-occipital |
| 8 | 63 | F | Glioblastoma multiforme | Right parieto-occipital |
| 9 | 45 | M | Glioblastoma multiforme | Right frontal |
| 10 | 54 | M | Glioblastoma multiforme | Right temporal |
| 11 | 71 | F | Glioblastoma multiforme | Left temporal |
| 12 | 64 | M | Glioblastoma multiforme | Left temporal |
| 13 | 69 | M | Glioblastoma multiforme | Left parieto-occipital |
| 14 | 50 | M | Glioblastoma multiforme | Right parietal |
| 15 | 65 | M | Glioblastoma multiforme | Left temporo-occipital |
| 16 | 56 | F | Glioblastoma multiforme | Left occipital |
| 17 | 36 | M | Glioblastoma multiforme | Right fronto-parietal |
| 18 | 38 | F | Glioblastoma multiforme | Left parietal |

were performed using a three-dimensional radiofrequency (RF) spoiled ($T_1$-weighted) fast field echo (gradient echo) technique (TR/TE (msec) = 4.2/1.2, FOV = 250 mm, slice thickness = 6.0 mm, overlap = 3 mm, effective slice thickness = 3 mm (Fourier interpolation), slices = 25, matrix = 128 × 128). Three preliminary acquisitions were performed at flip angles of 2°, 10°, and 35° as precontrast data set to enable the calculation of $T_1$ maps. The DCE series ($T_1$dy) was carried out at a flip angle of 35° and consisted of a series of 60 volumes, with a temporal resolution of approximately six seconds. The CA (0.1 mmol/kg body weight of gadodiamide (Gd-DTPA-BMA; Nycomed, Oslo, Norway) was administered as a manual bolus injection over a period of approximately four seconds following the seventh dynamic scan. A flush of an equal amount of normal saline was given immediately afterward at the same injection speed.

### *Image Analysis*

All images were transferred to an independent workstation for analysis. FPLP analysis was carried out with two in-house-written IDL applications (Interactive Data Language®; Research Systems Inc., Boulder, CO). The modified TK analysis was performed with the use of an in-house-developed software package written in C under the Unix operating system (21) and the medical image viewer MRIcro® (Chris Rorden, Nottingham, UK).

#### *Theoretical Basis of the Models*

The leakage of the CA into the EES is described by the following equation:

$$v_e \frac{dC_e(t)}{dt} = K^{trans}(C_p(t) - C_e(t)). \quad (1)$$

where $v_e$ is the EES (as a fraction of voxel volume; $v_P$ = blood plasma space, $v_i$ = intracellular space, and $v_e + v_p + v_i = 1$), $C_e$ is the concentration of contrast in the EES, $C_p$ is the concentration of contrast in the blood plasma space, and $K^{trans}$ is the volume transfer constant. $K^{trans}$ depends on the permeability and surface area of the endothelium, as well as blood volume and flow in the measured voxel (22). In contrast to other tissues, healthy brain parenchyma $K^{trans}$ should be ≈0, because of the intactness of the BBB.

#### *Method 1*

The TK model (TK) was introduced in 1991 and has become a popular method for the assessment of $K^{trans}$. The VIF used in the current study is based on a previous work, in which blood samples were taken to enable assessment of the CA concentration time course in blood (23). The following equation was used to describe the observed biexponential decay:

$$C_p(t) = D[a_1\exp(-m_1t) + a_2\exp(-m_2t)] \quad (2)$$

where $D$ is the concentration of the administered CA, $a_1$ and $m_1$ are respectively the amplitude and rate constants of the fast exponential decay (contrast leakage into the interstitium), and $a_2$ and $m_2$ are respectively the amplitude and rate constants of the slow exponential decay (contrast excretion through the kidneys). We applied this biexponential VIF via the following general equation describing CA diffusion across a semipermeable barrier (16):

$$C_t(t) = K_{TK}\int_0^t C_p(t')\exp\left[\frac{-K_{TK}(t-t')}{v_e}\right]dt'. \quad (3)$$

where $K_{TK}$ is $K^{trans}$ as estimated by the TK model.

#### *Method 2*

We also analyzed the data with a modification of the TK technique (mTK) that aims to separate contrast en-

hancement effects within individual voxels due to contrast leakage into the EES from those due to intravascular contrast. This method applies an individually measured $C_p(t)$ from an automatically calculated AIF, and allows the fractional volume occupied by the blood plasma, $v_p$, to be estimated (5,16,21,22):

$$C_t(t) = v_p C_p(t) + K_{mTK} \int_0^t C_p(t') \exp\left[\frac{-K_{mTK}(t-t')}{v_e}\right] dt' \quad (4)$$

where $K_{mTK}$ is $K^{trans}$ as estimated by the mTK model. The automated AIF definition was applied to extract $C_p(t)$ from a slice including the middle cerebral artery, since this was the only major artery within the imaging volume.

*Method 3*

The FPLP model was designed to separate the signal increase due to intravascular CA from the signal increase due to increased capillary permeability. It allows independent calculation of maps of regional blood volume and the volume transfer constant, but not of EES. In contrast to methods 1 and 2, it is based on the first pass of the CA bolus. Therefore, for the purposes of this work, $K^{trans}$ is designated as $K^{trans}$-first pass or $K_{FP}$. As in the mTK technique (method 2), patient-specific VIFs are derived from purely vascular voxels to obtain $C_p(t)$, but are defined manually from the signal enhancement in the superior sagittal sinus rather than the middle cerebral artery. Toward that end, a region of interest (ROI) is drawn around the superior sagittal sinus in a dynamic image slice, preferably in the middle of the imaged volume to exclude inflow effects. The resulting first-pass portion of the vascular CA concentration curve is fitted to a gamma variate function:

$$C_P(t) = C_{P_{max}}(t - t_0)^b \exp\left[\frac{-(t-t_0)}{c}\right] \quad (5)$$

where $b$ and $c$ are arbitrary constants used for fitting.

Assuming that the backflow of the CA from the EES back to the intravascular compartment is negligible during the first pass of the CA bolus (by assuming that the ratio of $K^{trans}$ to $v_e$ is low, which is equivalent to assuming $C_p(t) > C_e(t)$), the concentration in the EES, as modeled in Eq. [3], can be reduced to

$$C_e(t) \approx \frac{K_{FP}}{V_e} \int_0^t C_p(t')\,dt' \quad (6)$$

This approximation of the EES concentration time course during the first pass is termed the "leakage profile." The CA concentration time course curve, $C_t(t)$, is then given by

$$C_t(t) = v_e C_e(t) + v_p C_p(t) = K_{FP} \int_0^t C_p(t')\,dt' + v_p C_p(t) \quad (7)$$

Hence, by measuring the area under the curve of the CA concentration time course in the EES and the intravascular space (i.e., a purely vascular voxel), one can calculate $K_{FP}$ (20). The assumption in the FPLP method that the ratio of $K^{trans}$ to $v_e$ is small has been shown to be the source of a systematic error that leads to underestimation when "true" $K^{trans}$ values are high. However, the method has demonstrated high accuracy when tested against $K_{TK}$, especially when "true" $K^{trans}$ values are low (19).

*Patient Studies*

All three methods were applied to calculate $K^{trans}$ and (whenever possible) $v_p$ and $v_e$, in two ROIs for each tumor studied (the whole tumor volume, and the enhancing part of the tumor volume after contrast administration). The whole-tumor ROIs were manually drawn by J.U.H., whereas the "enhancing ROIs" were calculated by an in-house-written IDL application with a threshold for "true" enhancement of one standard deviation above the mean enhancement of normal brain parenchyma. The enhancing regions were contained entirely within the tumor regions.

Analysis yielded calculations of the parameter maps and median values for all three models: $K_{TK}$ and $v_{eTK}$ from the TK model; $K_{mTK}$, $v_{emTK}$, and $v_{pmTK}$ from the mTK model; and $K_{FP}$ and $v_{pFP}$ from the first-pass technique.

The two software packages used had inherent differences in the definition of the VIF: the mTK technique used the middle cerebral artery, while the first-pass technique used the superior sagittal sinus. One consequence of this was that partial volume averaging errors in the arterial ROI resulted in underestimation of the AIF. We accounted for this by rescaling the AIF using the ratio of the maximum values of contrast concentration of the two VIFs. Subsequently, all parameter estimates of the FPLP technique were corrected using the individual scaling factor under the assumption that this would approximately correct for magnitude differences between the venous and arterial VIFs.

### *Statistics*

Friedman's test and Wilcoxon's signed-rank tests were applied to compare the median values of $K^{trans}$, $v_p$, and $v_e$ of the three models, and Spearman's correlation test was used to correlate those values. A $P$-value $< 0.05$ was considered statistically significant.

## RESULTS

A comparison of median $K^{trans}$ values obtained from the three different models showed no correlation between either $K_{FP}$ and $K_{TK}$ or $K_{mTK}$ and $K_{TK}$. The application of a threshold that excluded voxels with $K_{TK}$ estimates above 1.2 $min^{-1}$ (an arbitrary threshold meant to filter out voxels suffering from pseudopermeability effects) (24) resulted in a correlation of median $K_{TK}$ and $K_{mTK}$ of $\rho = 0.57$ ($P < 0.05$), whereas medians of thresholded $K_{TK}$ still did not show a significant correlation with median $K_{FP}$. Qualitative analyses of individual patient voxel-by-voxel scatter plots yielded the same results.

Figures 1 and 2 show scatter plots comparing $K_{FP}$ and $K_{TK}$ (Fig. 1) and $K_{mTK}$ and $K_{TK}$ (Fig. 2), including thresholded and unthresholded $K_{TK}$ estimates for all investigated patients. These plots also show that the median values of $K_{TK}$ were considerably higher than the median $K_{mTK}$ and $K_{FP}$ estimates ($P < 0.001$), with differences between the models of up to two orders of magnitude.

The median $K_{FP}$ estimated without scaling for software-dependent VIF differences, and $K_{mTK}$ were correlated with a correlation coefficient of $\rho = 0.62$ ($P < 0.01$). Scaling of $K_{FP}$ according to the patient's individual difference in VIFs improved the correlation to $\rho = 0.74$ ($P < 0.01$). A comparison of median $K_{FP}$ and $K_{mTK}$ estimates showed $K_{mTK}$ values to be generally higher, with $K_{FP}$ estimates ranging from 0.007 to 0.065 $min^{-1}$, and scaled $K_{FP}$ estimates ranging from 0.007 to 0.094 $min^{-1}$. $K_{mTK}$ had values of 0.028–0.142 $min^{-1}$. Figure 3a displays a scatter plot of median $K_{FP}$ and $K_{mTK}$ estimates for all patients with and without scaling of $K_{FP}$. Figure 3b–d shows pixel-by-pixel scatter plots of $K_{FP}$ vs. $K_{mTK}$ in three individual patients. Figure 4a shows a post-injection DCE $T_1$-weighted image of a high-grade glioma taken during the first passage of the CA bolus. Figure 4b–d show the corresponding $K_{FP}$, $K_{mTK}$, and $K_{TK}$ maps obtained from the respective models. A comparison of the maps clearly demonstrates the diversity in the distribution of values within the tumor and the normal brain. On $K_{FP}$ maps, the normal brain shows minimal values consistent with noise, while the tumor shows high values, especially in the enhancing rim. The only other intracranial structures showing significant high values of $K_{FP}$ are the choroid plexus and the meninges. In contrast to this, the $K_{TK}$ maps clearly show the effect of pseudopermeability, with high values seen in pixels that represent blood vessels (e.g., the distal branches of the middle cerebral artery and around the great cerebral veins). The $K_{mTK}$ map shows a pattern of distribution similar to that in the $K_{FP}$ map, with no evidence of residual pseudopermeability effects in vascular structures. The corresponding $v_{p(FP)}$ and $v_{p(mTK)}$ maps (Fig. 4e and f) obtained from the first-pass and mTK models show similarities with the $K_{TK}$ map due to the latter's contamination with erroneously identified vessels. The

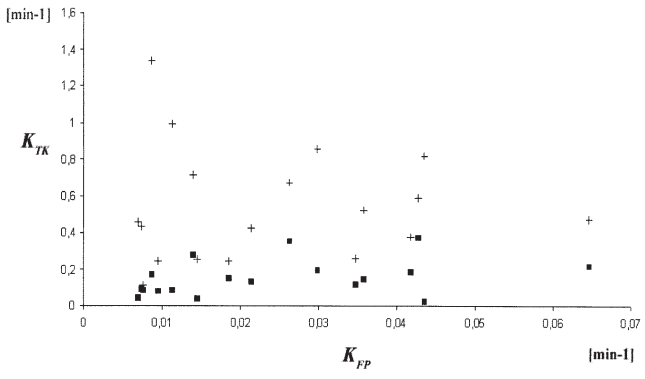


**Figure 1.** Scatter plot of $K_{FP}$ vs. $K_{TK}$ estimates for all patients. Crosses and squares represent unthresholded and thresholded estimates of $K_{TK}$, respectively. No correlation is seen between the unthresholded or thresholded estimates of $K_{TK}$ and $K_{FP}$.

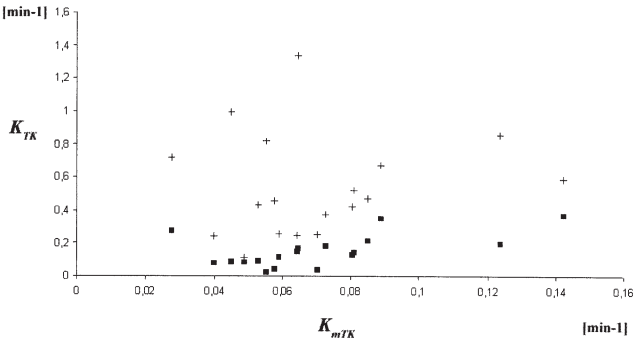


**Figure 2.** Scatter plot of estimates of $K_{mTK}$ vs. $K_{TK}$ for all patients, including unthresholded (crosses) and thresholded (squares) $K_{TK}$ estimates. After thresholding, $K_{mTK}$ and $K_{TK}$ correlate ($\rho = 0.57$, $P < 0.05$).

superior sagittal sinus, as well as other structures, can be detected on both images but is not seen on the corresponding $K_{FP}$ and $K_{mTK}$ map. Figure 5a–d shows typical VIFs acquired with the two techniques.

A comparison of median estimates of $v_p$ also showed a significant difference of $v_{p(mTK)}$ and scaled $v_{p(FP)}$ ($P < 0.001$); however, these values showed a very high correlation ($\rho = 0.901$; $P < 0.01$). Before $v_{p(FP)}$ was scaled to account for VIF differences, there were no significant differences in $v_p$ values, but there was also no significant correlation of the models. This indicates the vital impact the correct definition of the vascular input has on the data. Figure 6a shows a scatter plot of median estimates of unscaled and scaled $v_{p(FP)}$ vs. $v_{p(mTK)}$ for all patients, demonstrating their high correlation between scaled values of $v_{p(FP)}$ and $v_{p(mTK)}$. Figure 6b–d displays scatter plots of patient-specific pixel-by-pixel analyses of unscaled $v_p$ estimates. Each example shows a close pixelwise correlation of estimates of $v_{p(FP)}$ and $v_{p(mTK)}$, but varies between the patients in scaling (the slope of the scatter plots).

In contrast to the above results, in parts of the analyzed tumor volume of two patients, the mTK model and the first-pass model did not agree. In these areas, $K_{mTK}$ estimates were very high, while $K_{FP}$ estimates were particularly low. Although the corresponding $v_{pFP}$ maps identified these areas as vessels, they were not depicted on the $v_{pmTK}$ maps, and were shown to be areas of high contrast leakage on the $K_{mTK}$ maps.

## DISCUSSION

$T_1$-weighted DCE-MRI is widely used in research (15,17–22,25) and drug trial studies (26,27) to evaluate malignancies such as lung and breast cancers, prostate tumors, and brain neoplasms (25,28–30). Since cancer therapy has moved on toward antiangiogenic treatment, precise methods to evaluate and differentiate changes in vascularity and vascular permeability are needed (25,31). Blood volume and endothelial permeability are both possible surrogate markers of angiogenic activity in tumors (32). Evaluation of these parameters therefore represents an important monitoring tool during any antiangiogenic therapy, and can also be confidently expected to provide valuable clinical infor-

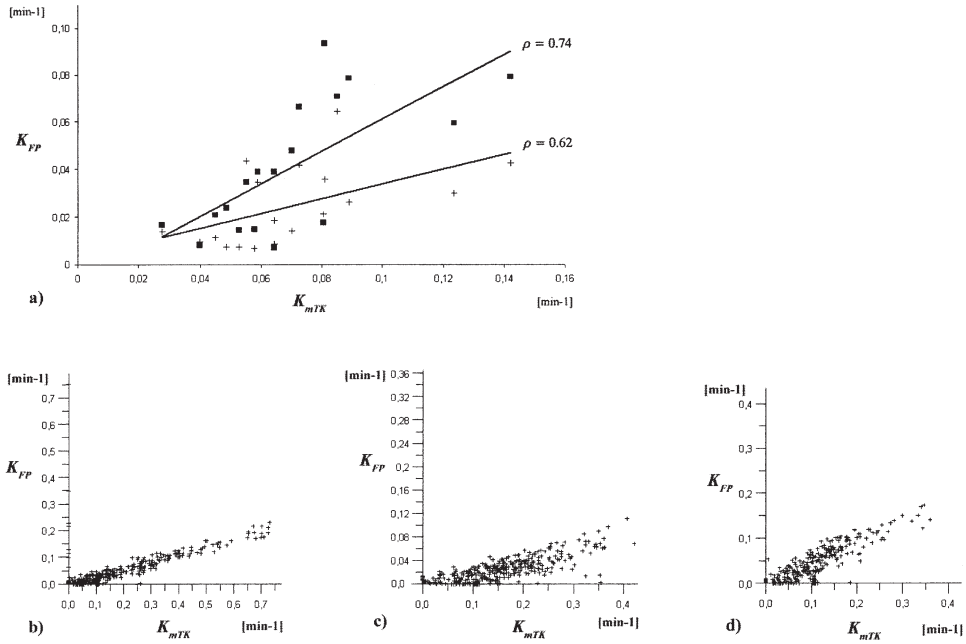


**Figure 3. a:** Scatter plot of median $K_{FP}$ and $K_{mTK}$ estimates of all patients before (crosses) and after (squares) scaling for differences between the maximum values of the input functions obtained with the first-pass and mTK models. The correlation improves after scaling (ρ = 0.62 before and ρ = 0.74 after scaling; $P$ = 0.01 for both correlations). $K_{FP}$ estimates are consistently lower than $K_{mTK}$ estimates. **b–d:** Scatter plots of a pixel-by-pixel analysis of $K_{FP}$ and $K_{mTK}$ for three patients, demonstrating the high correlation of the parameter estimates, which differ only in dimension.

mation for diagnosis, classification, and treatment planning (33).

Various kinetic models have been applied for the analysis of $T_1$-weighted DCE-MR images, the best-established model being the one described by Tofts and Kermode (3) in 1991. The main disadvantage of this model is that it overestimates $K^{trans}$ in highly vascularized regions, since the contribution of intravascular CA to the signal enhancement is mistaken as tracer that enters the EES and thus appears to reflect permeability. Hence, failure of this model (i.e., the pseudopermeability effect) is to be expected in tissues with dense vascularity, as commonly found in malignant tumors. A further weak point of the TK model is that it uses a standardized VIF. Originally derived from a study published by Weinmann et al (23), the model assumes biexponential decay for the plasma contrast concentration curve after bolus administration of a CA (3). Weinmann et al (23) collected serial blood samples over 120 minutes to measure Gd-DTPA plasma levels, sampling the first three of a total of 10 blood tests at one, three, and eight minutes after administration of the CA. Although this approximation is convenient for DCE-MRI studies, since it is more challenging to obtain accurate measurements of CA in major blood vessels than in static tissue, it is in fact likely to be inaccurate. The true configuration of the intravascular contrast concentration time course is ignored, since the contribution of the first pass of the CA bolus is not sampled. Hence, important information is lost—particularly in tumor studies (22). Currently, the high temporal resolution of dynamic MRI and the availability of methods that are largely insensitive to inflow effects allow measurement of the first-pass peak, which should therefore be taken into account when perfusion and endothelial permeability are evaluated (34).

Together with the technical advances in MRI, an enormous variety of analysis approaches have been described in the last decade. For research and clinical purposes, it is crucial to understand the advantages and disadvantages of the applied model or analysis method, especially when comparing data that have been acquired with different techniques. All three models considered in this work can be described as compartmental models that differ mainly in assumptions regarding VIFs (4,5,10,20). Distributed parameter models. such as that proposed by St. Lawrence and Lee (35) (a modification of the tissue homogeneity model introduced by Johnson and Wilson (36)) and also used by Henderson et al (13), Buckley (10), and others, are more sophisticated and, given a suitable data acquisition, allow estimation of tissue blood flow, capillary permeability-surface area product, $v_e$, and $v_p$ (22). In the compartmental models we used for this work, the parameter $K^{trans}$ is the product of the CA extraction fraction ($E$) and blood flow ($F$) (6,22). Therefore, in a situation where permeability is high, $K^{trans}$ is limited by the tissue blood flow, whereas if there is no flow limitation, $K^{trans}$ depends principally on the vascular permeability (via the relationship $E = 1 - \exp(-PS/(F(1 - \mathrm{Hct}))$, where $PS$ is the permeability capillary wall surface area product, and Hct is the hematocrit). A distributed parameter model enables the measurement of both $PS$ and $F$, and is therefore likely to produce information that is more easily interpreted at the physiological level (35). On the other hand, estimating an increasing number of parameters leads to increasing instability of a model and difficulty in model fitting, especially when the SNR is low (10).

In this study, we aimed to compare three compartmental-model approaches: the conventional TK model, a first-pass technique, and the mTK model. The latter two models were designed to avoid the above-described pseudopermeability effect. Both techniques include the measurement of a patient-specific VIF, and allow estimation of both $K^{trans}$ and $v_p$. Since it is assumed that the backflow of the CA from the EES to the intravascular compartment during the first pass of the CA bolus is

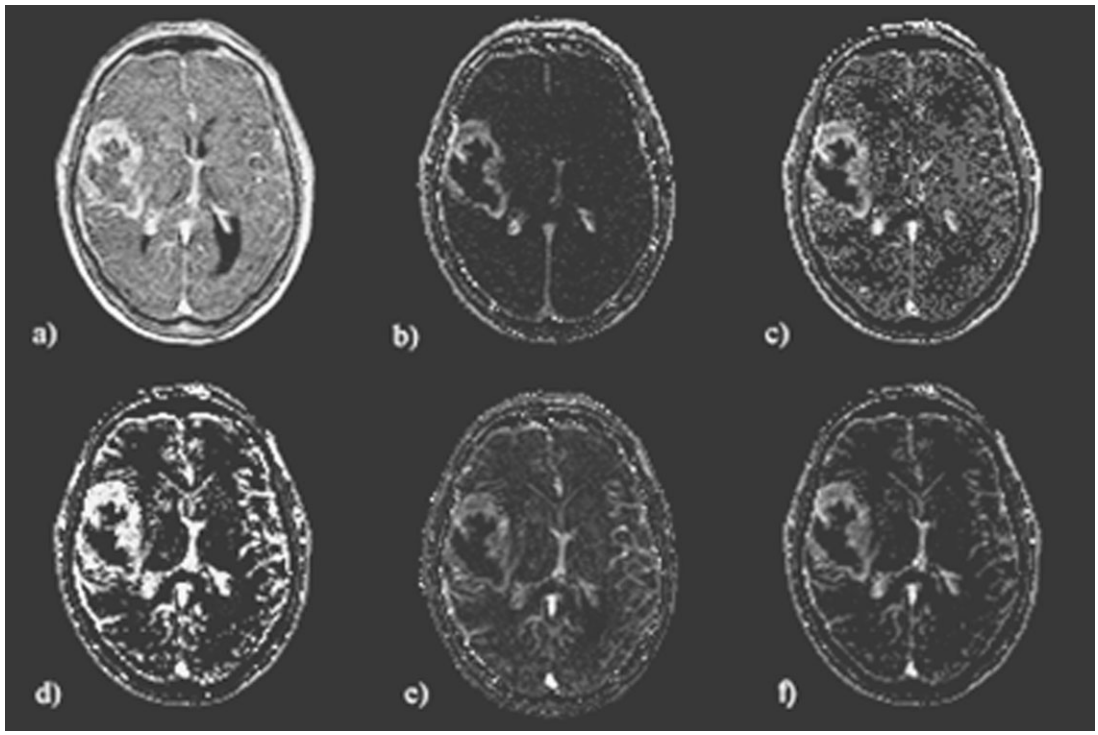


**Figure 4. a:** DCE $T_1$-weighted image of a high-grade glioma acquired during the first passage of the CA bolus (10 seconds post-injection). Enhancement is seen in the superior and inferior sagittal sinuses, and the choroid plexus of the posterior horns of the lateral and third ventricles. The tumor is located in the right temporo-parietal region and shows glioma-typical rim enhancement. **b:** The corresponding $K_{FP}$ map generated with the first-pass model. **c** and **d:** The corresponding $K_{mTK}$ and $K_{TK}$ maps. The $K_{FP}$ and $K_{mTK}$ maps show hardly any enhancement; vessels are seen on the corresponding dynamic image, and enhancement is shown mainly in the tumor, the highly-leaky choroid plexus, and the meninges. In contrast, the $K_{TK}$ map displays both vessel enhancement and leakage, demonstrating the pseudopermeability effect. **e** and **f:** $\upsilon_{pFP}$ and $\upsilon_{pmTK}$ maps of the same patient. Both maps display the vessels that are seen in the dynamic image correctly, as well as the choroid plexus; however, the $\upsilon_{pmTK}$ map is noisier than the $\upsilon_{pFP}$ map. Window settings are the same for all parametric maps, except for the $K_{TK}$ maps, where scaling by a factor of 3 was needed to display the whole range of values.

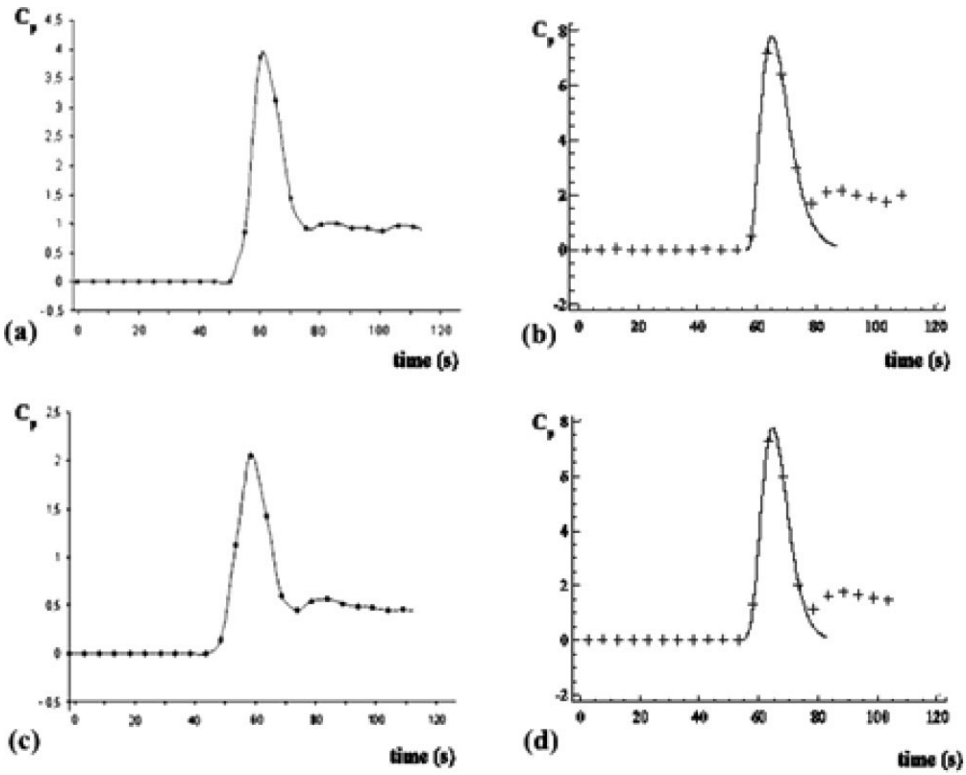


**Figure 5.** Vascular input functions of two patients: (**a** and **b**) patient 1, and (**c** and **d**) patient 2. **a** and **c:** Unfitted VIFs derived from the middle cerebral artery (mTK technique). **b** and **d:** Fitted VIFs derived from the superior sagittal sinus (FPLP technique).

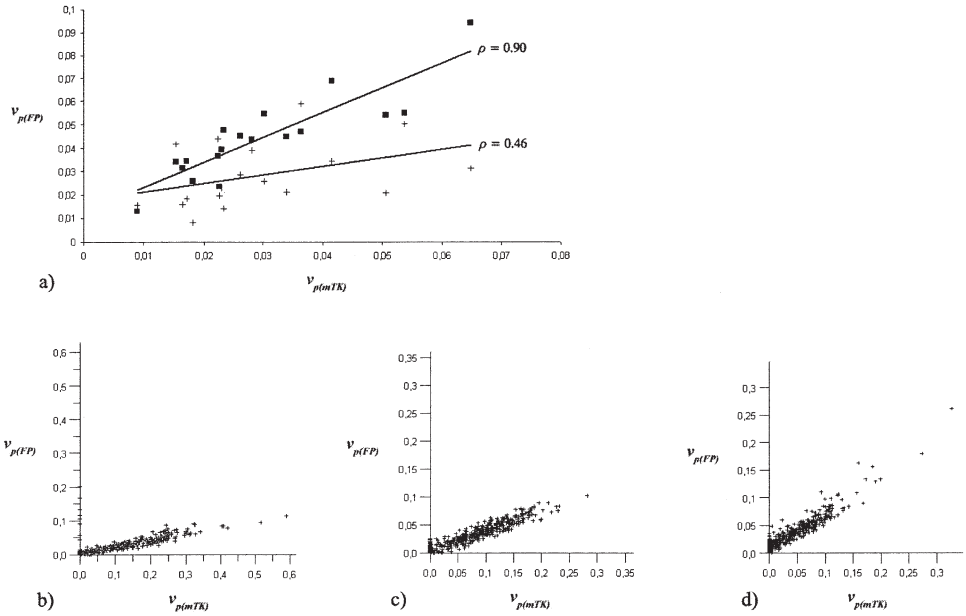


**Figure 6. a:** Scatter plot of median estimates of unscaled and scaled $v_{p(FP)}$ and $v_{p(mTK)}$ for all patients. A high correlation ($\rho = 0.90$; $P = 0.01$) is demonstrated between the two estimates after scaling (squares), whereas before scaling (crosses) no correlation is seen at all. **b–d:** Scatter plots of a patient-specific pixel-by-pixel analysis of $v_p$ estimates of the same patients as in Fig. 3b–d, demonstrating the high intra-individual correlation for this parameter between the two techniques. Differences are found only in the slope of the plot. Axes are not labeled, since $v_p$ represents a fraction (blood plasma volume per unit volume of tissue).

negligible, the FPLP does not allow measurement of $v_e$. High-grade gliomas were chosen as the tissue of interest because these tumors are among the most vascularized tumors known in humans, and they commonly exhibit a great degree of vascular permeability. High-grade gliomas have therefore been intensively studied with perfusion and permeability mapping techniques, including PET, SPECT, ultrasound, CT, and MRI (18,25,37–39).

The results of the present study show that the mTK model and the first-pass technique provide similar results for estimating blood plasma volume and $K^{trans}$, and at the same time avoid pseudopermeability effects. As shown in previous modeling and clinical studies, the conventional TK model yielded $K_{TK}$ values that were spuriously high, reaching two orders of magnitude of $K_{FP}$ values, while the corresponding $K_{TK}$ maps clearly demonstrated numerous vessels (10,11,19). It is therefore not surprising that there was no correlation between $K_{TK}$ and $K_{FP}$ and/or $K_{TK}$ and $K_{mTK}$. The application of a threshold excluding $K_{TK}$ values of $>1.2$ min$^{-1}$ led to a weak correlation of $K_{TK}$ and $K_{mTK}$ ($\rho = 0.571$, $P < 0.05$), whereas no significant correlation was observed between $K_{TK}$ and $K_{FP}$. Nonetheless, the application of a threshold is unsatisfactory because many pixels below the threshold will still suffer from pseudopermeability and thus yield inaccurate permeability maps, since the model itself does not account for signal enhancement due to intravascular CA. These considerations indicate a general lack of specificity in the information provided by the TK model.

Although estimates of $K_{FP}$ and $K_{mTK}$ showed a good correlation ($\rho = 0.744$), $K_{mTK}$ still had consistently higher values than $K_{FP}$ ($K_{FP} \approx 0.6 * K_{mTK}$), even after patient-specific scaling for differences in the VIF of either model was performed. Input functions that were acquired from superior sagittal sinus for the first-pass model had higher maximum values in 14 of 18 patients than the corresponding input function obtained from the middle cerebral artery for the extended TK model. However, the shape of the curves was always very similar. This difference is most likely due to partial volume effects that affect the input function obtained from the middle cerebral artery, since this vessel is significantly smaller than the superior sagittal sinus. However, differences in inflow effects between the two sites could also cause a significant difference in the measured amplitude of the VIF. Furthermore, due to the design of the analysis software, the input functions from the middle cerebral artery were acquired automatically (which has been shown to be reproducible in this setting (21)), whereas the input functions from the superior sagittal sinus were collected after an ROI was manually positioned in that vessel. As part of the FPLP software, the latter were also fitted to a Gamma variate (which effectively regularizes the AIF), which also explains the reduced noise on the corresponding $K_{FP}$ maps. It seemed reasonable to account for the difference between the input functions, since the vascular contribution represents a fundamental part of both models with a high impact on the resulting $K^{trans}$ and $v_p$ values. Since we aimed to compare kinetic models, and not dissimilarities resulting from the differences between the VIFs, the scaling should have minimized these differences. Obviously, the influence of the different input functions could only have been ruled out if the same input functions had been used for each model, which was not possible given the available software.

The remaining, non-input-function-dependent differences between $K_{FP}$ and $K_{mTK}$ must be explained by a mixture of genuine modeling differences and differences in the software implementation of the models. Although both models have a compartmental basis, the analysis approach of each one is different. While FPLP is based on a shape analysis that decomposes intravoxel signal into intra- and extravascular contributions, our implementation of the mTK model derives its parameter values by a best fit of Eq. [4] to the contrast concentration time course within each voxel. Furthermore, the mTK model allows estimation of the fractional

volume of the EES ($v_e$), which is unobtainable with the first-pass method. This is because of the assumption that the backflow of the CA from the EES back to the intravascular compartment is insignificant during the first pass of the CA bolus (in practice, the assumption is that the ratio $K^{trans}/v_e$ is small, implying $C_P > C_e$ during the first passage, and leading to Eq. [4] reducing to Eq. [6]). Besides resulting in the non-estimableness of $v_e$, this leads to a systematic underestimation of $K_{FP}$, which can become severe at high values of $K_{FP}$ (19). A voxel-by-voxel comparison of $K_{FP}$ and $K_{mTK}$ showed that in most patients both parameters correlated well, and the difference was just a question of scaling. However, in some tumors, areas of disagreement were found: $K_{mTK}$ estimates were relatively high, whereas the corresponding $K_{FP}$ estimates were particularly low. Corresponding $v_{pFP}$ maps showed vessels in these areas. These discrepancies highlight an interesting difference in interpretation of the time courses between the methods: while the first-pass model interprets the signal mainly as $v_p$, the mTK model has the freedom to assign such a time course to a high-$K^{trans}$, low-$v_e$ region (in other words, leaky vessels but negligible distribution volume), a scenario that would produce a similar pixel time course. Nevertheless, such discrepancies were observed in only two patients, and in general the degree of agreement between the models far outweighed the differences.

In contrast to the correlation between $K^{trans}$ estimates, the correlation of median estimates of $v_p$ depended very much on the scaling for VIF differences. Before scaling, a comparison of the median $v_{p(FP)}$ and median $v_{p(mTK)}$ estimates showed no correlation, whereas the intrapatient voxel-by-voxel analysis demonstrated a very high correlation. Interindividual differences were found between the scaling relation of $v_{p(FP)}$ and $v_{p(mTK)}$, such that in seven of 18 patients $v_{p(FP)}$ was higher than $v_{p(mTK)}$, while in the remaining 11 patients the scaling relation was the other way around. This explains the missing interindividual correlation between the median estimates when no scaling factor that corrects for differences in the size of the VIF is used. After the difference of the VIFs was corrected for, the correlation of median $v_{p(FP)}$ and median $v_{p(mTK)}$ became high ($\rho = 0.90$), although first-pass estimates of $v_p$ were consistently higher than the estimates obtained with the mTK technique ($v_{p(FP)} \approx 1.6 * v_{pmTK}$). Buckley (10) demonstrated in a study on simulated data that the mTK model consistently underestimated true values of $v_p$ by 2–96% (10), which could partially explain the differences we observed between $v_{p(FP)}$ and $v_{p(mTK)}$. On the other hand, estimates of $v_{p(FP)}$ may be erroneously high in cases in which the basic assumption of the first-pass model—that $v_e$ is negligible during the first-pass of the CA bolus—is incorrect. However, the voxel-by-voxel analysis of $v_{p(FP)}$ estimates did not show a significant correlation with $v_{e(mTK)}$, which suggests that there was no major influence of $v_e$ on $v_{p(FP)}$, assuming that the mTK model gave correct values for $v_e$. In some patients there was a correlation of $v_{e(mTK)}$ and $K_{FP}$; however, since the same correlation was found for $v_{e(mTK)}$ and $K_{mTK}$, a coincidence of genuine high $v_e$ and high $K^{trans}$ in some areas of the tumor has to be assumed.

These results clearly emphasize the impact of the *individual* VIF, and the importance of determining this function to account for the vascular signal contribution. The use of a standardized VIF, as in the TK model, therefore jeopardizes any data analysis that is used to obtain accurate estimates of microvascular variables. The lack of correlation of the standard TK parameters with those defined with the use of more sophisticated models implies that this approach should perhaps be regarded as somewhat heuristic in its description of CA kinetics in tumors.

In summary, we have shown that two available models that are intended to allow explicit modeling of $v_p$ effectively remove pseudopermeability effects. The excellent correlation between the two models of estimates of $K^{trans}$ and $v_p$, together with the results of previous simulation studies (19), allow us to conclude that both models are valid for evaluating perfusion and permeability in tumors. The reduced time needed to acquire data when the first-pass model is applied is potentially useful, especially in abdominal studies, because it makes breath-hold image acquisitions more feasible. This may also be a benefit for head studies conducted in patients with low tolerability for the MRI environment.

## ACKNOWLEDGMENTS

We thank Xiaoping Zhu and Kaloh Li, who developed the FPLP method and wrote the software for implementing it at our center, and Dave Chaplin, who developed the software for the parametric comparison. J.U. Harrer was supported by the German Society of Clinical Neurophysiology and Functional Imaging.

## REFERENCES

1. Lopes MB. Angiogenesis in brain tumors. Microsc Res Technol 2003;60:225–230.
2. Birner P, Piribauer M, Fischer I, et al. Vascular patterns in glioblastoma influence clinical outcome associate with variable expression of angiogenic proteins: evidence for distinct angiogenic subtypes. Brain Pathol 2003;13:133–143.
3. Tofts PS, Kermode AG. Measurement of the blood-brain barrier permeability and leakage space using dynamic MR imaging. I. Fundamental concepts. Magn Reson Med 1991;17:357–367.
4. Larsson HB, Stubgaard M, Sondergaard L, Henriksen O. In vivo quantification of the unidirectional influx constant for Gd-DTPA diffusion across the myocardial capillaries with MR imaging. J Magn Reson Imaging 1994;4:433–440.
5. Daldrup HE, Shames DM, Husseini W, Wendland MF, Okuhata Y, Brasch RC. Quantification of the extraction fraction for gadopentetate across breast cancer capillaries. Magn Reson Med 1998; 40:537–543.
6. Tofts PS, Brix G, Buckley DL, et al. Estimating kinetic parameters from dynamic contrast-enhanced T(1)-weighted MRI of a diffusable tracer: standardized quantities and symbols. J Magn Reson Imaging 1999;10:223–232.
7. Brix G, Semmler W, Port R, Schad LR, Layer G, Lorenz WJ. Pharmacokinetic parameters in CNS Gd-DTPA enhanced MR imaging. J Comput Assist Tomogr 1991;15:621–628.
8. Tofts PS, Berkowitz B, Schnall MD. Quantitative analysis of dynamic Gd-DTPA enhancement in breast tumors using a permeability model. Magn Reson Med 1995;33:564–568.
9. Galbraith SM, Lodge MA, Taylor NY, et al. Reproducibility of dynamic contrast-enhanced MRI in human muscle and tumours: comparison of quantitative and semi-quantitative analysis. NMR Biomed 2002;15:132–142.
10. Buckley DL. Uncertainty in the analysis of tracer kinetics using dynamic contrast-enhanced T(1)-weighted MRI. Magn Reson Med 2002;47:601–606.

11. Haroon HA, Buckley DL, Patankar TA, et al. A comparison of Ktrans measurements obtained with conventional and first pass pharmacokinetic models in human gliomas. J Magn Reson Imaging 2004; 19:527–536.
12. Parker GJM, Suckling J, Tanner SF, et al. Probing tumor microvascularity by measurement, analysis and display of contrast agent uptake kinetics. J Magn Reson Imaging 1997;7:564–574.
13. Henderson E, Sykes J, Drost D, Weinmann HJ, Rutt BK, Lee TY. Simultaneous MRI measurement of blood flow, blood volume, and capillary permeability in mammary tumors using two different contrast agents. J Magn Reson Imaging 2000;12:991–1003.
14. Evelhoch JL. Key factors in the acquisition of contrast kinetic data for oncology. J Magn Reson Imaging 1999;10:254–259.
15. Rijpkema M, Kaanders JHAM, Joosten FBM, van der Kogel AJ, Heerschap A. Method for the quantitative mapping of dynamic MR contrast agent uptake in human tumors. J Magn Reson Imaging 2001;14:457–463.
16. Tofts PS. Modelling tracer kinetics in dynamic Gd-DTPA MR imaging. J Magn Reson Imaging 1997;7:91–101.
17. Jackson A, Haroon H, Zhu XP, Li KL, Thacker NA, Jayson G. Breath-hold perfusion and permeability mapping of hepatic malignancies using magnetic resonance imaging and a first-pass leakage profile model. NMR Biomed 2002;15:164–173.
18. Li KL, Zhu XP, Checkley DR, et al. Simultaneous mapping of blood volume and endothelial permeability in gliomas using iterative analysis of first-pass dynamic contrast-enhanced MRI data. Br J Radiol 2002;76:39–50.
19. Li KL, Jackson A. A new hybrid method for accurate and reproducible quantitation of dynamic contrast-enhanced MRI data. Magn Reson Med 2003;50:1286–1295.
20. Li KL, Zhu XP, Waterton J, Jackson A. Improved 3D quantitative mapping of blood volume and endothelial permeability in brain tumors. J Magn Reson Imaging 2000;12:347–357.
21. Parker GJ, Jackson A, Waterton JC, Buckley DL. Automated arterial input function extraction for T1-weighted DCE-MRI. In: Proceedings of the 11th Annual Meeting of ISMRM, Toronto, Canada, 2003. p 1264.
22. Parker GJM, Padhani AR. $T_1$-weighted dynamic contrast enhanced MRI. In: Tofts PS, editor. Quantitative MRI of the brain, 2003. Chichester: John Wiley and Sons Ltd.; 2003. p 341–364.
23. Weinmann H-J, Laniado M, Mützel W. Pharmacokinetics of Gd-DTPA/dimeglumine after intravenous injection into healthy volunteers. Physiol Chem Physics Med NMR 1984;16:167–172.
24. Jackson A, Jayson GC, Li KL, et al. Reproducibility of quantitative dynamic contrast-enhanced MRI in newly presenting glioma. Br J Radiol 2003;76:153–162.
25. Padhani AR, Husband JE. Dynamic contrast-enhanced MRI studies in oncology with an emphasis on quantification, validation and human studies. Clin Radiol 2001;56:607–620.
26. Jayson GC, Zweit J, Jackson A, et al. Molecular imaging and biological evaluation of HuMV833 anti-VEGF antibody: implications for trial design of antiangiogenic antibodies. J Natl Cancer Inst 2002;94:1484–1493.
27. Knopp MV, Giesel FL, Marcos H, von Tengg-Kobligk H, Choyke P. Dynamic contrast-enhanced magnetic resonance imaging in oncology. Top Magn Reson Imaging 2001;12:301–308.
28. Hunter GJ, Hamberg LM, Choi N, Jain RK, McCloud T, Fischman AJ. Dynamic T1-weighted magnetic resonance imaging and positron emission tomography in patients with lung cancer: correlating vascular physiology with glucose metabolism. Clin Cancer Res 1998; 4:949–955.
29. Buckley DL, Roberts C, Parker GJM, et al. Prostate cancer: evaluation of vascular characteristics with dynamic contrast-enhanced T1-weighted MR imaging–initial experience. Radiology 2004; in press.
30. Zhu XP, Li KL, Kamaly-Asl ID, et al. Quantification of endothelial permeability, leakage space, and blood volume in brain tumors using combined T1 and T2* contrast-enhanced dynamic MR imaging. J Magn Reson Imaging 2000;11:575–585.
31. Robinson SP, McIntyre DJ, Checkley D, et al. Tumour dose response to the antivascular agent ZD6126 assessed by magnetic resonance imaging. Br J Cancer 2003;88:1592–1597.
32. McDonald DM, Choyke PL. Imaging of angiogenesis: from microscope to clinic. Nat Med 2003;9:713–725.
33. Padhani AR. Functional MRI for anticancer therapy assessment. Eur J Cancer 2002;38:2116–2127.
34. Fritz-Hansen T, Rostrup E, Larsson HBW, Sondergaard L, Ring P, Henriksen O. Measurement of the arterial concentration of Gd-DTPA using MRI: a step towards quantitative perfusion imaging. Magn Reson Med 1996;36:225–231.
35. St. Lawrence KS, Lee TY. An adiabatic approximation to the tissue homogeneity model for water exchange in the brain: I. Theoretical derivation. J Cereb Blood Flow Metab 1998;18:1365–1377.
36. Johnson JA, Wilson TA. A model for capillary exchange. Am J Physiol 1966;210:1299–1303.
37. Tamura M, Shibasaki T, Zama A, et al. Assessment of malignancy of glioma by positron emission tomography with 18-F-flourodeoxyglucose and single photon emission tomography with thallium-201 chloride. Neuroradiology 1998;40:210–215.
38. Harrer JU, Mull M, Mayfrank L, Klötzsch C. Second harmonic imaging: a new ultrasound technique to assess human brain tumour perfusion. J Neurol Neurosurg Psychiatry 2003;74:333–338.
39. Cenic A, Nabavi DG, Craen RA, Gelb AW, Lee T-Y. A CT method to measure hemodynamics in brain tumors: validation and application of cerebral blood flow maps. Am J Neuroradiol 2000;21:462–470.